

## The first target experiments on the National Ignition Facility

O.L. Landen<sup>1,a</sup>, S.H. Glenzer<sup>1</sup>, D.H. Froula<sup>1</sup>, E.L. Dewald<sup>1</sup>, L.J. Suter<sup>1</sup>, M.B. Schneider<sup>1</sup>, D.E. Hinkel<sup>1</sup>, J.C. Fernandez<sup>2</sup>, J.L. Kline<sup>2</sup>, S.R. Goldman<sup>2</sup>, D.G. Braun<sup>1</sup>, P.M. Celliers<sup>1</sup>, S.J. Moon<sup>1</sup>, H.S. Robey<sup>1</sup>, N.E. Lanier<sup>2</sup>, S.G. Glendinning<sup>1</sup>, B.E. Blue<sup>1</sup>, B.H. Wilde<sup>2</sup>, O.S. Jones<sup>1</sup>, J. Schein<sup>1</sup>, L. Divol<sup>1</sup>, D.H. Kalantar<sup>1</sup>, K.M. Campbell<sup>1</sup>, J.P. Holder<sup>1</sup>, J.W. McDonald<sup>1</sup>, C. Niemann<sup>1</sup>, A.J. Mackinnon<sup>1</sup>, G.W. Collins<sup>1</sup>, D.K. Bradley<sup>1</sup>, J.H. Eggert<sup>1</sup>, D.G. Hicks<sup>1</sup>, G. Gregori<sup>1</sup>, R.K. Kirkwood<sup>1</sup>, B.K. Young<sup>1</sup>, J.M. Foster<sup>3</sup>, J.F. Hansen<sup>1</sup>, T.S. Perry<sup>1</sup>, D.H. Munro<sup>1</sup>, H.A. Baldis<sup>1</sup>, G.P. Grim<sup>2</sup>, R.F. Heeter<sup>1</sup>, M.B. Hegelich<sup>2</sup>, D.S. Montgomery<sup>2</sup>, G.A. Rochau<sup>7</sup>, R.E. Olson<sup>7</sup>, R.E. Turner<sup>1</sup>, J.B. Workman<sup>2</sup>, R.L. Berger<sup>1</sup>, B.I. Cohen<sup>1</sup>, W.L. Kruer<sup>1</sup>, A.B. Langdon<sup>1</sup>, S.H. Langer<sup>1</sup>, N.B. Meezan<sup>1</sup>, H.A. Rose<sup>2</sup>, C.H. Still<sup>1</sup>, E.A. Williams<sup>1</sup>, E.S. Dodd<sup>2</sup>, M.J. Edwards<sup>1</sup>, M.-C. Monteil<sup>5</sup>, R.M. Stevenson<sup>3</sup>, B.R. Thomas<sup>3</sup>, R.F. Coker<sup>2</sup>, G.R. Magelssen<sup>2</sup>, P.A. Rosen<sup>3</sup>, P.E. Stry<sup>1</sup>, D. Woods<sup>1</sup>, S.V. Weber<sup>1</sup>, P.E. Young<sup>1</sup>, S. Alvarez<sup>1</sup>, G. Armstrong<sup>1</sup>, R. Bahr<sup>6</sup>, J.-L. Bourgade<sup>5</sup>, D. Bower<sup>1</sup>, J. Celeste<sup>1</sup>, M. Chrisp<sup>1</sup>, S. Compton<sup>1</sup>, J. Cox<sup>1</sup>, C. Constantin<sup>1</sup>, R. Costa<sup>1</sup>, J. Duncan<sup>1</sup>, A. Ellis<sup>1</sup>, J. Emig<sup>1</sup>, C. Gautier<sup>2</sup>, A. Greenwood<sup>1</sup>, R. Griffith<sup>1</sup>, F. Holdner<sup>1</sup>, G. Holtmeier<sup>1</sup>, D. Hargrove<sup>1</sup>, T. James<sup>1</sup>, J. Kamperschroer<sup>1</sup>, J. Kimbrough<sup>1</sup>, M. Landon<sup>1</sup>, F.D. Lee<sup>1</sup>, R. Malone<sup>4</sup>, M. May<sup>1</sup>, S. Montelongo<sup>1</sup>, J. Moody<sup>1</sup>, E. Ng<sup>1</sup>, A. Nikitin<sup>1</sup>, D. Pellinen<sup>4</sup>, K. Piston<sup>1</sup>, M. Poole<sup>1</sup>, V. Rekow<sup>1</sup>, M. Rhodes<sup>1</sup>, R. Shepherd<sup>1</sup>, S. Shiromizu<sup>1</sup>, D. Voloshin<sup>1</sup>, A. Warrick<sup>1</sup>, P. Watts<sup>4</sup>, F. Weber<sup>1</sup>, P. Young<sup>1</sup>, P. Arnold<sup>1</sup>, L. Atherton<sup>1</sup>, G. Bardsley<sup>1</sup>, R. Bonanno<sup>1</sup>, T. Borger<sup>1</sup>, M. Bowers<sup>1</sup>, R. Bryant<sup>1</sup>, S. Buckman<sup>1</sup>, S. Burkhart<sup>1</sup>, F. Cooper<sup>1</sup>, S.N. Dixit<sup>1</sup>, G. Erbert<sup>1</sup>, D.C. Eder<sup>1</sup>, R.E. Ehrlich<sup>1</sup>, B. Felker<sup>1</sup>, J. Fornes<sup>1</sup>, G. Frieders<sup>1</sup>, S. Gardner<sup>1</sup>, C. Gates<sup>1</sup>, M. Gonzalez<sup>1</sup>, S. Grace<sup>1</sup>, T. Hall<sup>1</sup>, C.A. Haynam<sup>1</sup>, G. Heestand<sup>1</sup>, M.A. Henesian<sup>1</sup>, M. Hermann<sup>1</sup>, G. Hermes<sup>1</sup>, S. Huber<sup>1</sup>, K. Jancaitis<sup>1</sup>, S. Johnson<sup>1</sup>, B. Kauffman<sup>1</sup>, T. Kelleher<sup>1</sup>, T. Kohut<sup>1</sup>, A.E. Koniges<sup>1</sup>, T. Labiak<sup>1</sup>, D. Latray<sup>1</sup>, A. Lee<sup>1</sup>, D. Lund<sup>1</sup>, S. Mahavandi<sup>1</sup>, K.R. Manes<sup>1</sup>, C. Marshall<sup>1</sup>, J. McBride<sup>1</sup>, T. McCarville<sup>1</sup>, L. McGrew<sup>1</sup>, J. Menapace<sup>1</sup>, E. Mertens<sup>1</sup>, J. Murray<sup>1</sup>, J. Neumann<sup>1</sup>, M. Newton<sup>1</sup>, P. Opsahl<sup>1</sup>, E. Padilla<sup>1</sup>, T. Parham<sup>1</sup>, G. Parrish<sup>1</sup>, C. Petty<sup>1</sup>, M. Polk<sup>1</sup>, C. Powell<sup>1</sup>, I. Reinbachs<sup>1</sup>, R. Rinnert<sup>1</sup>, B. Riordan<sup>1</sup>, G. Ross<sup>1</sup>, V. Robert<sup>1</sup>, M. Tobin<sup>1</sup>, S. Sailors<sup>1</sup>, R. Saunders<sup>1</sup>, M. Schmitt<sup>1</sup>, M. Shaw<sup>1</sup>, M. Singh<sup>1</sup>, M. Spaeth<sup>1</sup>, A. Stephens<sup>1</sup>, G. Tietbohl<sup>1</sup>, J. Tuck<sup>1</sup>, B.M. Van Wonterghem<sup>1</sup>, R. Vidal<sup>1</sup>, P.J. Wegner<sup>1</sup>, P. Whitman<sup>1</sup>, K. Williams<sup>1</sup>, K. Winward<sup>1</sup>, K. Work<sup>1</sup>, R. Wallace<sup>1</sup>, A. Nobile<sup>2</sup>, M. Bono<sup>1</sup>, B. Day<sup>2</sup>, J. Elliott<sup>1</sup>, D. Hatch<sup>2</sup>, H. Louis<sup>1</sup>, R. Manzenares<sup>2</sup>, D. O'Brien<sup>1</sup>, P. Papin<sup>2</sup>, T. Pierce<sup>2</sup>, G. Rivera<sup>2</sup>, J. Ruppe<sup>1</sup>, D. Sandoval<sup>2</sup>, D. Schmidt<sup>2</sup>, L. Valdez<sup>2</sup>, K. Zapata<sup>2</sup>, B.J. MacGowan<sup>1</sup>, M.J. Eckart<sup>1</sup>, W.W. Hsing<sup>1</sup>, P.T. Springer<sup>1</sup>, B.A. Hammel<sup>1</sup>, E.I. Moses<sup>1</sup>, and G.H. Miller<sup>1</sup>

<sup>1</sup> Lawrence Livermore National Laboratory, P.O. Box 808, Livermore, CA 94550, USA

<sup>2</sup> Los Alamos National Laboratory, Los Alamos, NM 87544, USA

<sup>3</sup> Atomic Weapons Establishment, Chilton, UK

<sup>4</sup> Bechtel Nevada, Livermore, CA 94550, USA

<sup>5</sup> Commissariat à l'Énergie Atomique, Bruyères-Le-Châtel, France

<sup>6</sup> Laboratory for Laser Energetics, Rochester, NY 14623, USA

<sup>7</sup> Sandia National Laboratory, Albuquerque, NM 87185, USA

Received 3 January 2006 / Received in final form 18 February 2006

Published online 18 May 2006 – © EDP Sciences, Società Italiana di Fisica, Springer-Verlag 2007

**Abstract.** A first set of shock timing, laser-plasma interaction, hohlraum energetics and hydrodynamic experiments have been performed using the first 4 beams of the National Ignition Facility (NIF), in support of indirect drive Inertial Confinement Fusion (ICF) and High Energy Density Physics (HEDP). In parallel, a robust set of optical and X-ray spectrometers, interferometer, calorimeters and imagers have been activated. The experiments have been undertaken with laser powers and energies of up to 8 TW and 17 kJ in flattop and shaped 1–9 ns pulses focused with various beam smoothing options. The experiments have demonstrated excellent agreement between measured and predicted laser-target coupling in foils and hohlraums, even when extended to a longer pulse regime unattainable at previous laser facilities, validated the predicted effects of beam smoothing on intense laser beam propagation in long scale-length plasmas and begun to test 3D codes by extending the study of laser driven hydrodynamic jets to 3D geometries.

**PACS.** 52. Physics of plasmas and electric discharges – 52.57.-z Laser inertial confinement – 52.38.-r Laser-plasma interactions

<sup>a</sup> e-mail: landen1@llnl.gov

## 1 Introduction

The National Ignition Facility (NIF) that is currently under construction [1] is a 192 laser beam system that is designed to deliver up to 1.8 MJ of energy at a wavelength of  $\lambda = 351$  nm on target. The laser is designed to first achieve ignition by indirect drive ICF [2] and to be used for a variety of HEDP experiments [3, 4] and basic science studies. The first 4 beams of NIF commissioned in 2003 have been used to exercise the unique laser capabilities of the facility, activate a variety of optical and X-ray target diagnostics, and perform an initial set of direct-drive and indirect-drive experiments as a first step towards future full NIF ICF and HEDP experiments.

We have activated experimental capabilities in four major areas. In support of future equation-of-state studies, we have demonstrated long steady shock propagation by using precisely tailored pulse-shapes. Specifically, a steady shock front speed corresponding to a 14 Mbar pressure was maintained over a duration of 3 ns. In the area of laser-plasma interactions, the effects of laser beam smoothing by spectral dispersion (SSD) and polarization smoothing (PS) on the beam propagation in long scale gas-filled targets has been studied at plasma scales relevant to indirect drive low  $Z$  filled ignition hohlraum designs [5]. The latest long scale gas-filled target experiments have shown propagation over 7 mm of low  $Z$  plasma without filamentation and beam break up when using full laser smoothing. In the area of hohlraum energetics, we have verified hohlraum radiation temperature scaling with laser power and hohlraum size to make contact with hohlraum experiments performed at the NOVA and Omega laser facilities. The vacuum hohlraums yielded low laser backscattering, and the hohlraum radiation temperature measured with an 18-channel Dante soft X-ray power diagnostic agreed well with radiation-hydrodynamics LASNEX calculations [6–8]. From time-resolved hard X-ray imaging, time-integrated hard X-ray spectroscopy [9] and coronal radiation measurements, we have validated analytical models and LASNEX calculations of long pulse hohlraum plasma filling [7, 8]. We also demonstrated understanding of the energetics of a high-contrast, long pulse, low  $Z$  gas-filled hohlraum drive of the type used for ignition [10, 11]. In the area of hydrodynamics, we have extended the study of high-Mach number hydrodynamic jets of astrophysical and ICF interest to 3D geometries [12]. The resulting jet features and space resolved transverse areal densities were diagnosed by point projection radiography from multiple views and used to validate new 3D codes [13].

Section 2 describes the general target chamber, diagnostic, and laser configuration and capabilities. Section 3 describes the specific experimental set-up and key results from each of the campaigns. We summarize in Section 4.

## 2 First quad NIF experimental set-up

Figure 1 shows the beam and target chamber layout used for the first NIF experiments. The first 4 beams of NIF entered the target chamber grouped in a quad (Q31B)

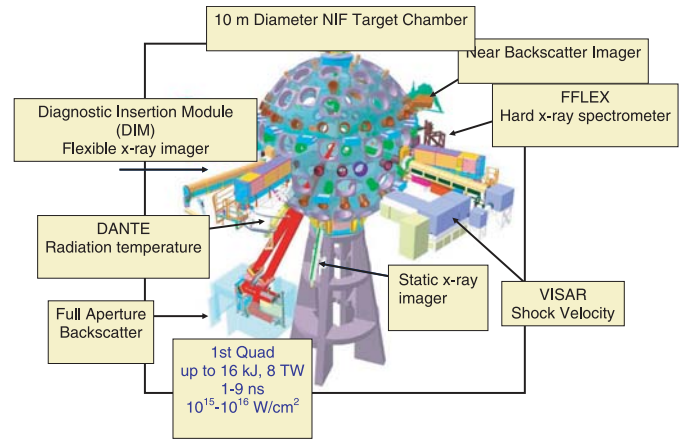


**Fig. 1.** Experimental layout of first 4 beams and diagnostics in the NIF target chamber.

from below at average polar coordinates  $\theta = 150^\circ$ ,  $\phi = 236.5^\circ$ , forming an  $\approx f/8$  cone of four  $f/20$  beams. The targets were inserted from the equator ( $\theta = 90^\circ$ ,  $\phi = 239^\circ$ ) and aligned using the 3 orthogonal axes of motion, pitch and roll.

The optical diagnostics included:

- (1) a dual channel sensitivity 670 nm line-imaging VISAR [14] whose distribution and collection optics were inserted in one of two Diagnostic Instrument Manipulators (DIM) at  $\theta = 90^\circ$ ,  $\phi = 45^\circ$ . The reflected laser pulses were sent to 2 interferometers and 2 optical streak cameras;
- (2) full aperture backscatter stations (FABS) [15, 16] on all 4 beams consisting of calorimeters, power meters, streaked spectrometers, absolutely calibrated time-integrated spectrometers, and near-field imagers analyzing reflected and backscattered pulses partially transmitted back through the final  $1\omega$  mirrors;
- (3) a Near Backscatter Imager (NBI) [17] consisting of calorimeters and imaging cameras viewing a well characterized diffuse reflector at the target chamber wall around ( $6^\circ$  to  $11^\circ$ ) and between individual beams of Q31B.

The X-ray diagnostics included:

- (4) a  $>2$  keV static X-ray imager (SXI) [18] consisting of a pinhole array, filters and X-ray CCD located at  $\theta = 161^\circ$ ,  $\phi = 326.5^\circ$ ;
- (5) an absolutely calibrated [19] 18-channel soft X-ray power diagnostic (“Dante”) covering the photon energy range of 50 eV to 10 keV [20] located at  $\theta = 143.25^\circ$ ,  $\phi = 274^\circ$ ;
- (6) an absolutely calibrated time-integrating 8-channel 10–100 keV hard X-ray calorimeter [21] located at  $\theta = 90^\circ$ ,  $\phi = 110^\circ$ ;
- (7) a 1D imaging 2–10 keV X-ray streak camera (SXD) insertable in the other DIM located at  $\theta = 90^\circ$ ,  $\phi = 315^\circ$ ;
- (8) a gated single or multiple frame 2–10 keV hard X-ray (FXI-HXRI) [22] and 0.5–2 keV soft X-ray (FXI-SXRI) 2D imager insertable in the DIM located at  $\theta = 90^\circ$ ,  $\phi = 315^\circ$ .

The experiments were undertaken with  $3\omega$  laser powers and energies of up to 8 TW and 17 kJ in flattop and shaped 1–9 ns pulses focused with various beam smoothing options (Continuous Phase-Plates (CPP), Polarization Smoothing (PS) and Smoothing by Spectral Dispersion (SSD)). CPPs installed in either near the front end or end of the  $1\omega$  amplification section of the laser provided  $n = 5$  super-Gaussian spots of either 0.25, 0.5 or 0.7 mm spot size ( $1/e$  point) [23]. PS provided by four wedged birefringent KDP crystals [24] separated orthogonal polarizations by  $30\ \mu\text{m}$  (more than a speckle size), reducing the number of highest intensity speckles that are most prone to filamentation (e.g. at  $>4\times$  the mean intensity) by  $2\times$ . SSD provided up to 90 GHz bandwidth at a 17 GHz modulation frequency. The  $3\omega$  laser energies and powers were measured with 2% time-integrated and 3%/ns time-resolved accuracy by calorimeters, diodes and for at least 1 beam, an optical streak camera.

For the framing and streak cameras, the data recording medium was a custom-designed 4k by 4k  $9\ \mu\text{m}$ -pixel CCD [25], while the SXI used a back-thinned X-ray sensitive  $24\ \mu\text{m}$  pixel 2k by 2k chip. The beam synchronization was set to 6 ps rms by comparing the timing of streaked 2 keV 1D images [26] of four separate 200 ps laser-plasmas created by the four beams impinging on a gold disk. The pointing accuracy for the pulsed beams was verified to be better than  $75\ \mu\text{m}$  rms from SXI images of the four laser-plasmas at 6–8 mm defocus ( $400\ \mu\text{m}$  spot size) impinging on a gold disk equipped with spatial fiducials.

All raw and in some cases partially analyzed data was available within five minutes after the shots. The experimental campaigns using the NIF first quad totaled  $\approx 60$  target shots spread over four 3–4 week long campaigns, with up to 3 shots fired per day at a maximum frequency of one shot every 3 h and routinely at once every 4–5 hours.

## 3 Experiments

### 3.1 Shock propagation

The purpose of the shock propagation experiments were to commission the VISAR diagnostic and demonstrate long, steady shock generation by planar direct-drive in support of future Equation-of-State (EOS) studies. Figure 2a shows the target design that used a plastic ablator, a mid- $Z$  doped preheat shield, and an aluminum witness plate for impedance matching to a smaller transparent quartz sample. A mJ-level,  $\mu\text{second}$  duration 670 nm VISAR beam impinges normally onto the quartz and surrounding aluminum. The VISAR beam is expected to reflect first off the aluminum exit surface and then off the central portion of the shock front as it propagates through the quartz. Since the target normal was set to face the bisector of the 4 NIF drive beams to ensure best, symmetric coupling, a planar mirror at a distance of 5 mm of the quartz was required to redirect the incident and reflected VISAR beam arriving along the chamber equator. The

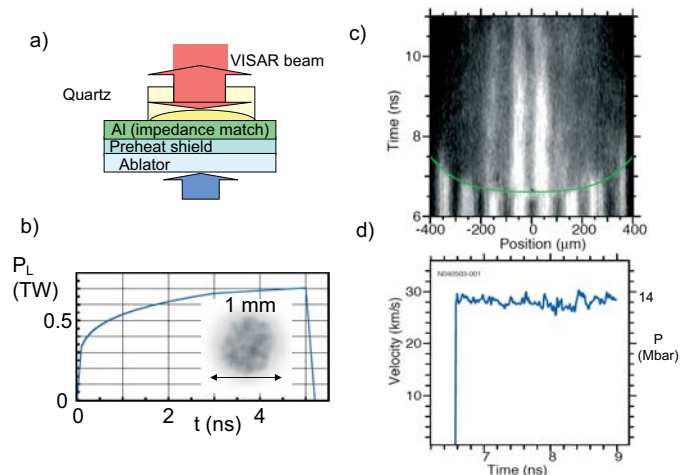


**Fig. 2.** (a) Target for long shock propagation experiment, (b) pulse-shape, (c) VISAR data, (d) shock velocity vs. time.

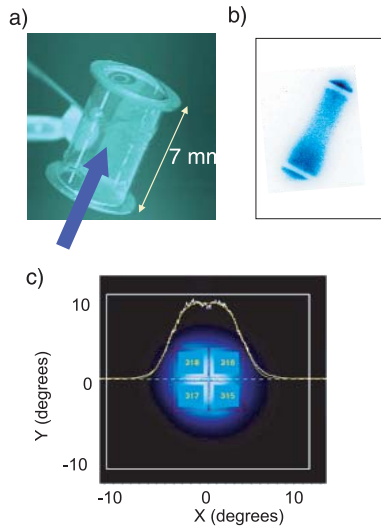
NIF drive beams were incident onto the ablator as overlapped CPP-smoothed  $700\ \mu\text{m}$  FWHM spots with a total energy of 3.3 kJ. Simulations were used to design a constant shock velocity resulting in a requested and delivered power profile gently rising in time over 5 ns (see Fig. 2b).

Figure 2c shows an example of the streaked absolutely timed VISAR fringes, showing an abrupt fringe shift at  $\approx 6.7$  ns as the shock enters the quartz and thereafter minimal fringe shift as would be expected for a constant shock velocity. Figure 2c also shows that the expected and measured shock break-out delay vs radial position (i.e. shock curvature) agree and met the requirement of shock planarity to 5% over  $500\ \mu\text{m}$  for future EOS measurements. Figure 2d plots the inferred shock velocity vs. time, showing shock (pressure) steadiness to better than 3% (6%), exceeding requirements for high-pressure EOS measurements, and an average shock pressure of 14 Mbar, within 10% of preshot calculations (not shown). The limiting factor on the inferred shock steadiness is ascribed to residual vibrations in the VISAR optics which have since been resolved.

### 3.2 Laser-plasma interaction

The goals of the Laser-Plasma Interaction (LPI) experiments were to commission a variety of optical backscatter and near backscatter detectors, a gas-filled target capability and laser beam smoothing techniques such as CPPs, PS and SSD, and then study the effects of smoothing on beam propagation in gas-filled targets at plasma scales relevant to indirect drive low  $Z$  filled ignition hohlraum designs.

For the LPI studies the laser beams are propagated down the axis of 4–7 mm-long plastic tubes filled with  $\text{CO}_2$  at  $0.07n_c$  density (see Fig. 3a), where  $n_c = 9 \times 10^{21}\ \text{cm}^{-3}$  is the critical density for the laser wavelength used ( $\lambda_0$  of 351 nm). The 4–7 mm was chosen as brackets the path length encountered by the inner beams in ignition hohlraums and represents a  $2\text{--}3\times$  increase over



**Fig. 3.** (a) Gas-tube geometry for LPI study, (b) example of measured sideview of 3.5 keV plasma X-ray emission at  $t = 3.5$  ns, (c) example of reconstructed backscatter and near backscatter image (with CPP, PS and SSD).

low  $Z$  plasma transmission studies in prior gasbag experiments at Nova [27]. The four NIF laser beams enter the targets on the axis forming effectively an  $f/8$  beam. The beam best focus with CPP is placed in the target center providing an intensity profile spot with a radial profile that is approximated by a  $n = 5$  super-Gaussian with a 0.5 mm diameter ( $1/e$  points). For a total laser energy of 16 kJ in a flattop pulse with 3.5 ns length, intensities up to  $2 \times 10^{15}$  W/cm<sup>2</sup> are reached in the plasma. The laser propagation is inferred from laser plasma emission measured side-on with a 100  $\mu$ m, 100 ps resolution gated 12-frame X-ray camera filtered for 3–5 keV photon energies (example shown in Fig. 3b). The laser energy and spectra backscattered by Stimulated Brillouin and Raman Scattering (SBS, SRS) inside the laser final focusing lenses and outside the lenses within a 20° angle was measured with the FABS and NBI, respectively, as shown in Figure 3c.

Laser propagation in 7 mm long CO<sub>2</sub> plasma and laser backscattering were measured for laser beams smoothed using combinations of CPP, SSD and PS. Figures 4a and 4b show 3.5 keV side-view images of the plasma emission without and with SSD and PS, respectively. We find that the beams with PS and SSD (Fig. 4b) propagate through the 7 mm long plasma and burn through at  $t = 1.5$  ns in close agreement with the time calculated by LASNEX simulations (Fig. 4c) that include backscatter losses discussed below. By contrast, the images (Fig. 4a) from the case without PS and SSD show a reduction in propagation distance and radial spreading of the emission front. We attribute these differences to the additional smoothing provided by SSD and PS that suppresses plasma filamentation and beam spraying. A filamentation figure of merit  $Q$  can be derived by balancing speckle diffraction with ponderomotive self-focussing [28] and is

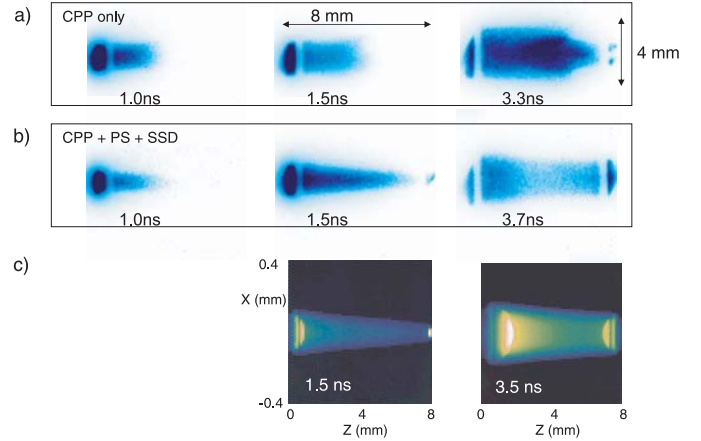


**Fig. 4.** Sequence of images of 3.5 keV X-ray emission. (a) Measured with CPP only, (b) measured with CPP, SSD and PS and (c) LASNEX post-processed simulation.

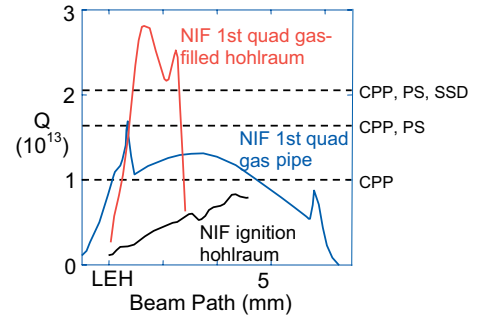


**Fig. 5.** Filamentation figure of merit in  $10^{13}$  units given by equation (1) for various laser-plasmas at peak intensity versus distance into plasma. Dashed lines are calculated filamentation thresholds for different laser beam smoothing options.

given by:

$$Q = I[\text{Wcm}^{-2}]\lambda^2[\mu\text{m}^2]n_e/n_c(3/T_e)[\text{keV}](\#/8)^2 \quad (1)$$

where  $Q$  is given in units of  $10^{13}$ ,  $I$  is the average laser intensity,  $\lambda$  the laser wavelength,  $n_e$  ( $T_e$ ) the electron density (temperature) and  $\#$  the beam  $f$  number. Figure 5 plots this filamentation figure of merit as a function of distance in the plasma at the peak of the pulse. In addition, 2-D and 3-D fine-scale simulations with the plasma interaction code pf3D [29,30] provide filamentation thresholds also shown in Figure 5 which increase as the level of smoothing is increased (i.e. as the number of high intensity speckles present for a given average laser intensity is decreased). We note that the gas-tube laser-plasma regime is above the threshold for CPP laser beam smoothing only ( $Q = 1$ ), but below the threshold with additional smoothing by PS and SSD ( $Q = 2.1$ ), explaining the reduction of laser beam spray and improvement in beam propagation for the latter case. By contrast, the conditions for the inner cone at peak drive for the ignition hohlraum are predicted to be below even the threshold for CPP only.

The measurements performed with FABS and NBI have shown that the backscattered light is mainly SBS.



Much of the scattered light is outside the lens apertures (i.e. on the NBI), partially attributable to backscattering that occurs after the onset of forward beam spraying. Moreover, the reconstructed combination of FABS data and NBI images (example shown in Fig. 3c) show that the laser is backscattered under a smaller solid angle when using CPP, SSD and PS for beam smoothing compared to when using CPP only, consistent with the reduced laser beam spraying, inferred from the gated X-ray images (Fig. 4).

Considerable laser backscattering levels of up to 40% (time-integrated) were measured in these  $T_e = 2$  keV (as inferred from SBS spectrum),  $T_i < 1$  keV (as calculated) long-scalelength plasmas. In line with previous experiments performed at similar laser intensities and plasma parameters on the NOVA and Omega laser facilities [2], the total laser backscattering was reduced to about 30% when using additional smoothing by SSD and PS. In ignition hohlraum designs, the electron temperature will be considerably higher (5 keV compared to  $\sim 2$  keV) and the laser intensity will be about twice lower ( $10^{15}$  W/cm<sup>2</sup> compared to  $2 \times 10^{15}$  W/cm<sup>2</sup>), yielding a much lower gain,  $G$ , for SBS and lower filamentation  $Q$  value as shown in Figure 5. As a consequence the beams inside ignition hohlraums are designed not to filament and the laser backscattering should be reduced. As a follow on to these 1st quad NIF experiments, current experiments at the Omega facility have now developed a higher  $T_e$  ( $>3$  keV) uniform density low  $Z$  plasma [31,32] to demonstrate this predicted reduction in backscatter at higher  $T_e$ .

### 3.3 Vacuum hohlraums

The goals of the vacuum hohlraum experiments were firstly to commission the soft X-ray diode array ‘‘Dante’’, the hard X-ray spectrometer FFLEX, and the hard X-ray hohlraum transmission and soft X-ray hohlraum burn-through imaging capability. Secondly, these experiments sought to make comparisons with prior Nova and Omega hohlraum data taken at similar incident laser power levels but with cones of many beams. Thirdly, these experiments sought to test the limits of hohlraum performance as set by plasma filling for either small enough hohlraums or long enough pulses.

For the vacuum hohlraum experiments we used cylindrical Au hohlraums of various sizes with a single laser entrance hole (LEH). The hohlraum back wall is irradiated with the four laser beams effectively forming an  $f/8$  cone that propagates along the hohlraum axis (see Fig. 6). Full aperture CPP and PS were installed on the laser beams providing a uniform intensity profile spot with either a 0.25 mm (for the smallest hohlraums) or 0.50 mm diameter with best focus placed at the LEH. Constant power (flattop) laser pulses with 100 ps rise and fall times were used with the following energy/pulse length combinations: 6 kJ/1.1 ns, 9 kJ/1.1 ns, 5 kJ/2 ns, 10 kJ/2 ns, 13 kJ/2 ns, 16 kJ/6 ns and 17 kJ/9 ns. Several hohlraum sizes were employed (0.56, 0.6, 1.2, 1.6 and 2.4 mm diameter with lengths 95–105% of their diameter). All but the smallest

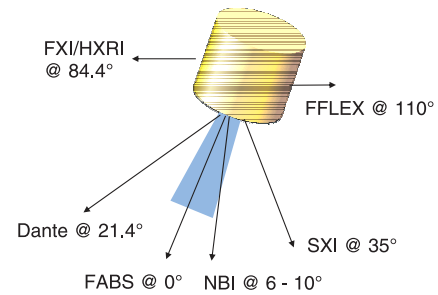


**Fig. 6.** Experimental set-up for single-ended hohlraum studies, showing diagnostic angular lines-of-sight relative to LEH normal.

Au hohlraum walls were 5  $\mu\text{m}$  thick, backed by a 100  $\mu\text{m}$  CH coating, allowing us to measure spatially resolved Au L-shell emission ( $>9$  keV) using the gated framing camera so as to infer the hohlraum plasma fill dynamics [33]. Dante has a partial view of the initial laser spots on the hohlraum back wall and provides a measure of the radiation flux that includes both the primary laser-plasma emission and the re-emitting walls. The hohlraum radiation temperature was inferred from the spectra integrals of the power measured by Dante through the LEH divided by the LEH area projection at 21.4°. The hot electron production inside the hohlraum was inferred using FFLEX. Similar to the LPI experiments, the total backscattered laser energy was measured with FABS and NBI. The static X-ray imager (SXI) confirmed that the beams propagated through the LEH without striking the outside walls of the hohlraum.

For all vacuum hohlraum experiments performed at intensities up to  $3 \times 10^{15}$  W/cm<sup>2</sup> the laser backscattering was negligible for both SRS ( $<0.05\%$ ) and SBS (0.6%). These backscattering values were roughly one order of magnitude smaller than those measured in vacuum hohlraum experiments performed at the Nova and Omega laser facilities at similar laser intensities, spatial laser beam smoothing, and peak hohlraum radiation temperatures [2]. This may be due to Nova and Omega vacuum hohlraums being irradiated by beams incident at 40° vs. normal to the hohlraum wall on NIF, leading to shorter effective scalelengths, higher flow gradients, and hence lower laser-plasma instability gain-length products for the NIF-case. Another possible explanation is the application of PS smoothing on NIF. Future experiments comparing backscattering with and without smoothing may help to better understand these observations.

The measured hot electron temperature was 30 keV and the fraction was  $< \sim 3\%$  in all hohlraums except the smallest, hohlraums irradiated at  $10^{16}$  W/cm<sup>2</sup> where it was 12%. The hot electron fraction increased with the laser intensity and for smaller hohlraums [9]. The SRS reflectivities increased with hot electron fraction indicating the Raman instability as major source of hot electrons, reaching a maximum of 3% for the smallest hohlraums. We also note that the inferred hot electron fraction for the lowest intensity shots at an ignition-relevant intensity

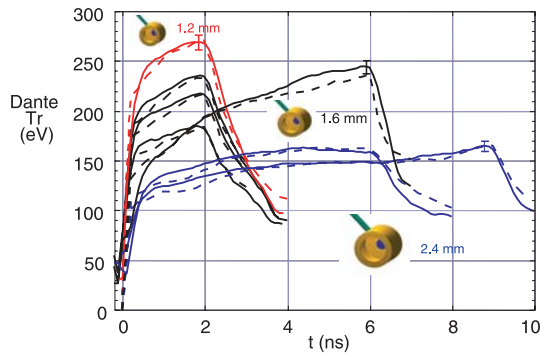


**Fig. 7.** Measured (solid lines) and calculated (dashed lines) radiation temperature time history for a variety of vacuum hohlraums driven by flattop pulses of 2, 6 and 9 ns duration.

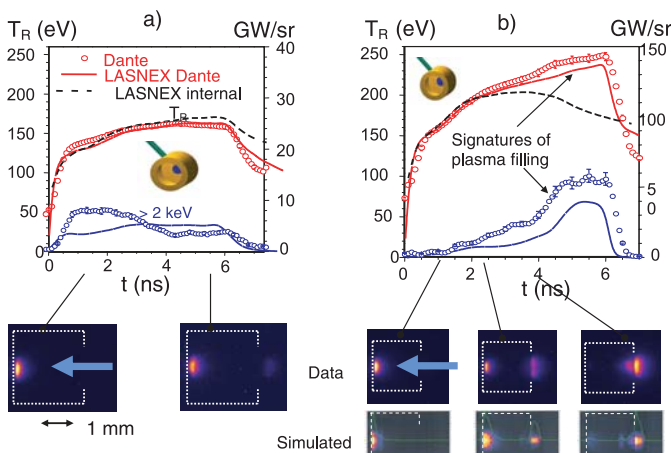


**Fig. 8.** Measured (solid lines) and calculated (dashed lines) radiation flux time history for 0.6-mm diameter vacuum hohlraums driven by 8.5 TW flattop pulse of 1.1 ns duration.

of  $1.5 \times 10^{15}$  W/cm<sup>2</sup> dropped precipitously to <1%, indicating favorable scaling for ignition.

Figure 7 shows the measured vs. post-processed LASNEX [34] simulations of the radiation temperature history  $Tr(t)$ . Dante and LASNEX calculated peak  $Tr$ 's agree within the experimental Dante radiation temperature error bar [19] of 2–3%, consistent with the insignificant losses due to backscatter and hot electrons that are not included in the simulations. The 2 ns, 1.6 mm diameter hohlraum data represents a regime similar to previous hohlraums [35–37] where minimal plasma filling is expected.

Hohlraum plasma filling [38,39] was revisited [7] using either longer laser pulses or smaller hohlraums. Figure 8 compares the measured and calculated Dante soft-X-ray fluxes, hard X-ray fluxes above 2 keV and thin wall images for the same drive (6 ns in 16 kJ) illuminating a 2.4 mm vs. a 1.6 mm diameter hohlraum. For the larger hohlraum, the Dante  $Tr$  and internal  $Tr$  that a package would see rise together, the hard X-ray coronal emission is relatively constant in time, and the majority of the hard X-ray emission remains near the back wall. By contrast, for the smaller hohlraum, we observe and predict several

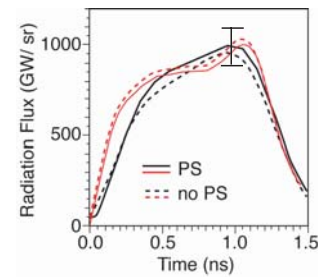


**Fig. 9.** Measured and calculated soft X-ray flux, >2 keV flux and hard X-ray (>9 keV) gated images for (a) 2.4 and (b) 1.6 mm diameter hohlraum heated by 2.7 TW, 6 ns laser pulse.

simultaneous signatures of significant plasma filling mid-way through the drive, namely a strong rise in hard X-ray flux, the emergence of significant emission at the LEH and the divergence of the internal and Dante  $Tr$ . The rise in Dante signals not seen for the larger hohlraum can hence be ascribed to the migration of the laser-plasma emission to the LEH where it is in full view by Dante. In addition, the onset of dense plasma filling was confirmed from the measured time delay and spectral shift of SRS [8] for the longer pulses.

Figure 9 compares measured vs. simulated Dante radiation flux for the smaller 0.6 mm hohlraums, also showing good agreement when including measured 10% backscatter losses. In this case, the addition of PS is predicted to slightly increase the soft X-ray flux, within Dante error bars. In terms of a radiation temperature, these small hohlraums reached 340 eV (including all flux which was observable out to 5 keV). A series of radiation burn-through images at about 1 keV photon energy were also collected using the FXI/SXRI, and are being compared to simulations for an independent assessment of the internal radiation temperature.

In addition to detailed numerical simulations, these results can be understood and extrapolated to higher laser energies and powers by applying a simple analytic model for radiation temperature limits [7]. This model is based on the increased hydrodynamic losses and coronal radiative losses [35] that occur when the laser absorption region migrates to the LEH as the hohlraum fills with plasma, leading to roll-over in the internal radiation temperature. In our model these losses become important at the LEH when the inverse bremsstrahlung absorption length in the laser heated LEH plasma becomes shorter than the LEH radius (i.e. when the laser-plasma and its emission is no longer effectively confined by the hohlraum). The plasma conditions for inverse bremsstrahlung are calculated by balancing X-ray ablated plasma pressure with laser heated plasma pressure and balancing heat conduction losses with inverse bremsstrahlung heating [40]. The model also balances hohlraum power in with Marshak wave wall losses, omitting thermal radiation losses out of the LEH that are less important for the LEH sizes used here. A constant X-ray conversion efficiency (C.E.) of 75% of the 100% absorbed laser energy is assumed, the later justified

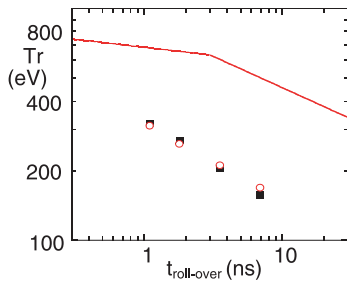


**Fig. 10.** Dante measured temperatures  $T_{LEH}$  at the roll-over time  $\tau$  (open circles) and the corresponding analytical limits (squares) calculated with equation (2) using experimental values of LEH radius  $r$  and laser power. Upper line is analytic model limit for a constant LEH radius  $r = 0.3$  mm for 600 TW, 1.8 MJ NIF hohlraum.

by the very low values of measured laser backscattering. The model gives the roll-over radiation temperature  $T_{max} = T_R(\tau)$  in terms of laser power or energy, roll-over time  $\tau$  and LEH radius  $r$ :

$$T_{max} = 1.0P_L^{0.20}/r^{0.20}\tau^{0.07} = 1.0E_L^{0.20}/r^{0.20}\tau^{0.27} \quad (2)$$

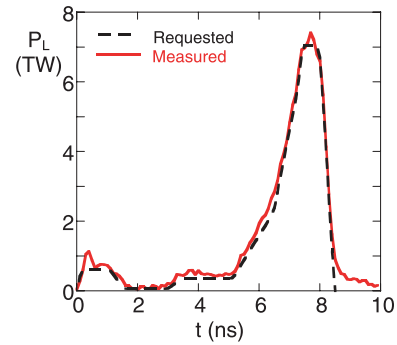
where  $T_{max}$  is in eV units, the flattop laser power (energy)  $P_L$  ( $E_L$ ) is in TW (kJ), the filling time  $\tau$  is in ns and the LEH radius  $r$  is in cm. The middle expression in equation (2) is applicable when the laser is power limited and the (right-hand) expression is applicable when the pulse length is long enough that the laser is energy limited.

Figure 10 plots the experimental Dante temperatures at the internal  $Tr$  roll-over times  $\tau$  and the corresponding  $T_{max}$  limits calculated with equation (2) showing good agreement. Figure 10 also shows the analytic predictions for  $T_R$  limits (Eq. (2)) imposed by plasma filling for future full NIF hohlraums assuming a minimum LEH radius of 0.3 mm, dictated by the minimum NIF laser spot size and a maximum angle of incidence of  $50^\circ$ .

### 3.4 Gas-filled hohlraums

The goals of the gas-filled hohlraum experiments were firstly to exercise a high contrast, long pulse low  $Z$  gas-filled hohlraum drive of the type that will be used for ignition hohlraums, and secondly, to study the laser energy coupling and tamping hydrodynamics [10].

The hohlraums consisted of 3 mm-long, 1.6 mm diameter 25  $\mu\text{m}$ -thick Au cylinders equipped with a 1.2 mm LEH and filled with either 1 atm. of  $\text{CO}_2$  or  $\text{C}_3\text{H}_8$  gas yielding 0.06–0.08 $n_c$  density. The 0.5 mm spot CPPs and PS were used with best focus placed at the LEH, yielding a peak intensity of  $3.5 \times 10^{15}$  W/cm<sup>2</sup>. Figure 11 compares the measured vs. requested 120:1 contrast 15 kJ pulse-shape, which was repeatably reproduced on this four shot series. The high contrast drive (ranging from 60 to 180 eV) required a dynamic range of over 1000 on some Dante channels, which was successfully accommodated by stitching the results from two oscilloscopes set at different sensitivities, a technique that will be also required for NIF



**Fig. 11.** Measured and requested high contrast pulse-shape used for gas-filled hohlraums.

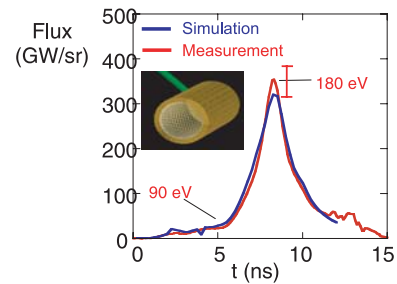


**Fig. 12.** Measured and calculated radiation flux history for gas-filled hohlraum.

ignition hohlraums. Figure 12 compares the measured vs. calculated Dante radiation flux, showing agreement within the 10% flux error bar [11]. The simulations account for the measured 25% backscatter and near-backscatter observed, predominantly SBS. The predominance of SBS was expected for the  $\text{CO}_2$  case with minimal ion Landau damping. The SBS predominance for the  $\text{C}_3\text{H}_8$  case with strong ion Landau damping was not easily predictable because various CH Nova LPI experiments resulted in either SRS [41] or SBS [36,42] dominance. The possible explanation for the turn-off of SRS and build-up of SBS in the current  $\text{C}_3\text{H}_8$  case is that the value of  $k\lambda_D$  exceeded 0.5 in the gas at peak power densities (0.06 $n_c$ ) and temperatures (3 keV), above the predicted cut-off for a collective electron SRS resonance [43]. This is a relevant finding as the NIF ignition hohlraum plasma values of  $k\lambda_D$  will also exceed 0.5 over much of the fill plasma. For these gas-filled hohlraums, we expected to exceed the filamentation threshold even with PS because of the combination of high laser intensity ( $3.5 \times 10^{15}$  W/cm<sup>2</sup> and low electron temperature ( $T_e < 4$  keV), as shown in Figure 5. This was corroborated by  $\approx 90\%$  of the scattered SBS light being collected by the NBI for these shots.

The hard X-ray imager provided clear images of the coronal plasmas, even through 25  $\mu\text{m}$  of gold, validating the hard X-ray imaging technique planned for ignition hohlraums with similar wall thicknesses. From the images we infer  $\approx 1$  mm of axial Au wall motion by the end of the pulse and a characteristic two-lobed emission profile attributed to the high density Au region near the wall and due to the colliding Au-gas front, in agreement with

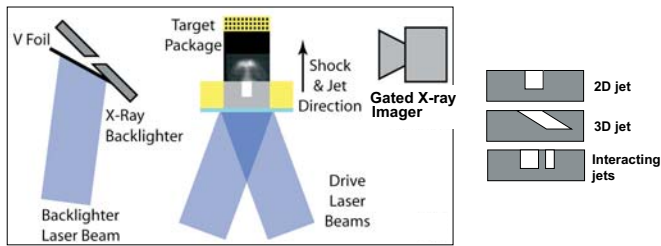


**Fig. 13.** Experimental set-up for hydrodynamic jet experiments.

simulations [44]. These results extend our validation of modeling of the Au wall tamping by a low  $Z$  fill to longer pulses, validation begun on Nova gas-filled hohlraums [45, 46].

### 3.5 Hydrodynamics

The goals of the hydrodynamics experiments were firstly to exercise X-ray backlighting capabilities on NIF, and secondly, to extend the study of hydrodynamic jets [47, 48] to 3D and multijet geometries for validating new 3D codes [49].

Figure 13 shows the experimental set-up. Two of the 4 NIF beams were used with a total of 6 kJ in 1.5 ns to drive a shock in a planar aluminum target. The drive beams were equipped with a CPP to produce the required flat-topped spot profile over  $700\ \mu\text{m}$ .  $200\ \mu\text{m}$ -scale holes of various geometries are implanted into the backside of the Al to promote corner jetting and subsequent breakout of a hydrodynamic Al jet into a foam reservoir. The relative alignment between drive beams and target was critical to produce symmetric jets; the measured rms shot-to-shot misalignment was  $60\ \mu\text{m}$ , better than the  $100\ \mu\text{m}$  functionality requirement for NIF. In addition, shot-to-shot drive beam energy was repeatable to 4%, also better than the 7% requirement.

A third beam was delayed by 16–22 ns using a special optical delay line installed after the beam is split into 4 and before final amplification. It was focused at 2 cm from chamber center on a V foil to produce a single pinhole-assisted [50–53] point projection 5.2 keV X-ray sidelit image per shot of the jets at  $20\ \mu\text{m}$  resolution. The images were recorded at  $20\times$  magnification by a single-frame  $3.5 \times 3.5\ \text{cm}$  version of a 200 ps gated FXI. Angled and side-by-side holes were used to provide a 3D geometry to compare to the single cylindrically symmetric 2D hole.

Figure 14 shows examples of sidelit data and post-processed Hydra [49] simulations at 22 ns from angled hole shots viewed from orthogonal directions on separate shots. We note the good left-right symmetry where expected, and qualitative agreement with simulations. It is interesting to note that even for this angled hole case, the jet direction remains normal to the target face and transverse center-of-mass of the jet and hole coincide, as calculated. Quantitative comparisons of mass ejected and speed of ejection with various code predictions is published elsewhere [12, 13, 54]. For the case of side-by-side jets, some unexpected interaction between the jets was

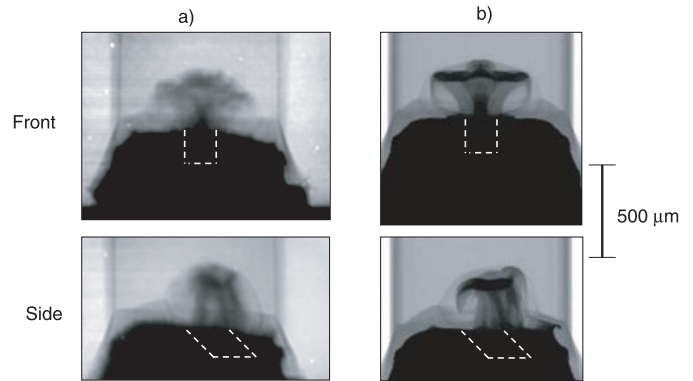


**Fig. 14.** Comparison of measured vs. calculated 3D hydrodynamic jet data.

observed, attributed to instability growth of small-scale initial roughness not included in the simulations.

## 4 Summary

A first set of ICF, HEDS and Basic Science-relevant experiments were performed using the first four beams of NIF. These first quad NIF experiments successfully exercised all existing facility capabilities and delivered new results. The experiments commissioned every type of optical and X-ray facility diagnostic. A planar, steady long pulse direct-drive capability was demonstrated. Good laser propagation with minimal filamentation and beam spray was demonstrated in long-scale length low  $Z$  plasma by using additional beam smoothing, in line with our understanding of the filamentation threshold. Vacuum hohlraums validated NIF hohlraum performance relative to prior facility hohlraum performance to the few % level over a wide range of radiation temperatures between 100 and 340 eV, probed limits due to plasma filling and validated a simple analytic hohlraum performance limit model. For the high contrast shaped-pulse gas-filled hohlraums, a self-consistent energetics budget was constructed in line with simulations, observations of wall tamping were matched by simulations, and new insights were gained on the competition between non-linear laser-plasma instabilities. Using orthogonal backlighting views, the study of hydrodynamic jet evolution was extended to 3D and dual features.

The many co-authors listed from the disciplines of target design, experiments, target diagnostic and laser science thank the NIF target area and laser operations crew for making these first experimental campaigns possible. This work was performed under the auspices of the U.S. Department of Energy by the University of California, Lawrence Livermore National Laboratory under Contract No. W-7405-ENG-48.

## References

1. G.H. Miller, E.I. Moses, C.R. Wuest, Nucl. Fusion **44**, 228 (2004)
2. J.D. Lindl et al., Phys. Plasmas **11**, 339 (2004)



3. M.D. Rosen, *Phys. Plasmas* **3**, 1803 (1996)
4. B.A. Remington et al., *Metall. Mater. Trans. A* **35A**, 2587 (2004)
5. S.H. Glenzer et al., *Nucl. Fusion* **44**, S185 (2004)
6. D.E. Hinkel et al., *Phys. Plasmas* **12**, 056305 (2005)
7. E.L. Dewald et al., *Phys. Rev. Lett.* **95**, 215004 (2005); E.L. Dewald et al., *Plasma Phys. Control. Fusion* **47**, B405 (2005)
8. E.L. Dewald et al., *Phys. Plasmas* **13**, 05xxxx (2006)
9. J.W. McDonald et al., *J. Phys. IV France* (to be published, 2006); J.W. McDonald et al., *Phys. Plasmas* **13**, 032703 (2006)
10. J.C. Fernandez et al., *Phys. Rev. Lett.* (submitted); J.C. Fernandez et al., *Phys. Plasmas* **13**, 05xxxx (2006)
11. J. Kline et al., *J. Phys. IV France* (to be published, 2006)
12. B.E. Blue et al., *Phys. Rev. Lett.* **94**, 095005 (2005)
13. B.E. Blue et al., *Phys. Plasmas* **12**, 056313 (2005)
14. P.A. Celliers et al., *Rev. Sci. Instrum.* **75**, 4916 (2004)
15. D.E. Bower et al., *Rev. Sci. Instrum.* **75**, 4177 (2004)
16. D.H. Froula et al., *Rev. Sci. Instrum.* **75**, 4168 (2004)
17. A.J. Mackinnon et al., *Rev. Sci. Instrum.* **75**, 4183 (2004)
18. M.D. Landon et al., *Rev. Sci. Instrum.* **72**, 698 (2002)
19. K.M. Campbell et al., *Rev. Sci. Instrum.* **75**, 3768 (2004)
20. E.L. Dewald et al., *Rev. Sci. Instrum.* **75**, 3759 (2004)
21. J.W. McDonald et al., *Rev. Sci. Instrum.* **75**, 3753 (2004)
22. K.S. Budil et al., *Rev. Sci. Instrum.* **68**, 796 (1997); H.F. Robey et al., *Rev. Sci. Instrum.* **68**, 792 (1997)
23. J.A. Menapace, S.N. Dixit, F.Y. Genin, W.F. Brocious, *Proc. SPIE* **5273**, 220 (2003)
24. D.H. Munro, S.N. Dixit, A.B. Langdon, J.R. Murray, *Appl. Opt.* **43**, 6639 (2004)
25. J. Kimbrough, J.D. Moody, P.M. Bell, O.L. Landen, *Rev. Sci. Instrum.* **75**, 4060 (2004)
26. O.L. Landen et al., *Rev. Sci. Instrum.* **66**, 788 (1995)
27. E. Williams, private communication
28. J.D. Moody et al., *Rev. Sci. Instrum.* **68**, 1725 (1997)
29. R.L. Berger et al., *Phys. Fluids B* **5**, 2243 (1993)
30. C.H. Still et al., *Phys. Plasmas* **7**, 2023 (2000)
31. C. Niemann et al., *J. Phys. IV France* (to be published, 2006)
32. D.H. Froula et al., *Phys. Plasmas* **13**, 05xxxx (2006)
33. L.J. Suter et al., *Rev. Sci. Instrum.* **68**, 838 (1997)
34. G.B. Zimmerman, W.L. Kruer, *Comm. Plasma Phys. Contr. Fusion* **2**, 51 (1975)
35. L.J. Suter et al., *Phys. Plasmas* **3**, 2057 (1996)
36. S.H. Glenzer et al., *Phys. Rev. Lett.* **80**, 2845 (1998); S.H. Glenzer et al., *Phys. Plasmas* **7**, 2585 (2000)
37. E. Dattolo et al., *Phys. Plasmas* **8**, 260 (2001)
38. G.D. Tsakiris, R. Sigel, *Phys. Rev. A* **38**, 5769 (1988)
39. R.M. Stevenson et al., *Phys. Plasmas* **11**, 2709 (2004)
40. J.D. Lindl, *Phys. Plasmas* **2**, 3933 (1995)
41. J.C. Fernández et al., *Phys. Rev. Lett.* **77**, 2702 (1996); J.C. Fernández et al., *Phys. Plasmas* **4**, 1849 (1997); J.C. Fernández et al., *Phys. Plasmas* **7**, 3743 (2000)
42. D.S. Montgomery et al., *Phys. Plasmas* **5**, 1973 (1998)
43. H.X. Vu et al., *Phys. Rev. Lett.* **86**, 4306 (2002); H.X. Vu et al., *Phys. Plasmas* **9**, 1745 (2002); D.S. Montgomery et al., *Phys. Rev. Lett.* **87**, 155001 (2001)
44. S.R. Goldman et al., *J. Phys. IV France* (to be published, 2006)
45. R.L. Kauffman et al., *Phys. Plasmas* **5**, 1927 (1998)
46. N.D. Delamater et al., *Phys. Plasmas* **7**, 1609 (2000)
47. J.M. Foster et al., *Phys. Plasmas* **9**, 2251 (2002)
48. M.M. Marinak et al., *Phys. Plasmas* **3**, 2070 (1996)
49. M.M. Marinak et al., *Phys. Plasmas* **8**, 2275 (2002)
50. O.L. Landen et al., *Rev. Sci. Instrum.* **72**, 627 (2001)
51. D.K. Bradley, O.L. Landen, A.B. Bullock, S.G. Glendinning, R.E. Turner, *Opt. Lett.* **27**, 134 (2002)
52. J. Workman et al., *Rev. Sci. Instrum.* **75**, 3915 (2004)
53. B.E. Blue, J.F. Hansen, H.F. Robey, *Rev. Sci. Instrum.* **75**, 3989 (2004)
54. B.E. Blue et al., *J. Phys. IV France* (to be published, 2006)